

RESEARCH ARTICLES

DYNAMIC ORDERING

Topology and dynamics of active nematic vesicles

Felix C. Keber,^{1,2*} Etienne Loiseau,^{1*} Tim Sanchez,^{3*} Stephen J. DeCamp,³ Luca Giomi,^{4,5} Mark J. Bowick,⁶ M. Cristina Marchetti,⁶ Zvonimir Dogic,^{2,3} Andreas R. Bausch^{1†}

Engineering synthetic materials that mimic the remarkable complexity of living organisms is a fundamental challenge in science and technology. We studied the spatiotemporal patterns that emerge when an active nematic film of microtubules and molecular motors is encapsulated within a shape-changing lipid vesicle. Unlike in equilibrium systems, where defects are largely static structures, in active nematics defects move spontaneously and can be described as self-propelled particles. The combination of activity, topological constraints, and vesicle deformability produces a myriad of dynamical states. We highlight two dynamical modes: a tunable periodic state that oscillates between two defect configurations, and shape-changing vesicles with streaming filopodia-like protrusions. These results demonstrate how biomimetic materials can be obtained when topological constraints are used to control the non-equilibrium dynamics of active matter.

Fundamental topological laws prove that it is not possible to wrap a curved surface with lines without encountering at least one singular point where the line is ill defined.

This mathematical result is familiar from everyday experience. Common examples are decorating Earth's surface with lines of longitude or latitude or covering a human hand with parallel papillary ridges (fingerprints). Both require the formation of singular points known as topological defects (1). The same mathematical considerations apply when assembling materials on microscopic length scales. Nematic liquid crystals are materials whose constituent rod-like molecules align spontaneously along a preferred orientation that is locally described by the director (line) field. Covering a sphere with a nematic leads to the formation of topological defects called disclinations. Mathematics dictates that the net topological charge of all defects on a spherical nematic must add up to +2, where a charge of s denotes a defect that rotates the director field by $2\pi s$. The basic nematic defects have charge $+1/2$ or $-1/2$, corresponding to a π rotation of the director field in the same sense or the opposite sense, respectively, as that of any closed path encircling the defect (2–6). Defects on topologically constrained geometries can acquire highly complex and tunable spatial arrangements, which

can drive assembly of intriguing higher-order hierarchical materials (7, 8). For this reason, combining conventional soft materials with topological constraints has emerged as a promising platform for organizing matter on micrometer length scales. So far, most studies in this area have focused on investigating equilibrium materials confined on rigid nondeformable surfaces of varying topology (9–17). Equilibrium statistical mechanics imposes tight constraints on the properties of such topological soft materials, which can acquire remarkable spatial complexity but cannot sustain persistent temporal dynamics.

Recent advances have enabled the assembly of active nematic liquid crystals in which the constituent rod-like building blocks continuously convert chemical energy into mechanical motion (18–20). Such materials are no longer constrained by the laws of equilibrium statistical mechanics. Consequently, unconfined active nematics exhibit highly sought-after properties such as spontaneous chaotic flows that are tightly coupled to continuously generating and annihilating motile defects (21–23). We have merged active nematics with soft topological constraints to create topological active matter. Microtubule-based active nematics were confined onto a deformable spherical surface provided by a lipid vesicle. Similar to well-studied equilibrium nematics confined on a sphere, topology requires the formation of defects with a net topological charge of +2. In stark contrast to the equilibrium case, however, activity generated by energy-consuming kinesin motors endows the active nematic defects with motility. As a result, the complex spatial defect structure becomes dynamic and the active nematic vesicles are turned into robust colloidal clocks with tunable frequency. By controlling the vesicle tension, we coupled the oscillatory dynamics of the active nematic cortex to vesicle deformations,

creating biomimetic shape-changing materials. Our experiments suggest a route for designing soft materials with controlled oscillatory dynamics. They further raise intriguing questions about how the dynamics of topological active matter can be enriched by increasing the complexity of the constraining surface, by controlling the nature of the synchronization transitions that occur in arrays of colloidal oscillators, and through the use of active crystals and other far-from-equilibrium materials (24).

Assembly of active nematic vesicles

We built on recent work by encapsulating active nematics into deformable vesicles. Active nematic vesicles encapsulating microtubules, kinesin motor clusters, and the nonadsorbing polymer polyethylene glycol (PEG) within a lipid vesicle were produced using an emulsion transfer technique (25). PEG induces adsorption of microtubule filaments onto the inner leaflet of the vesicle by the depletion mechanism (26). At high microtubule concentration, the entire vesicle surface is coated with a dense monolayer of extensile microtubule bundles, effectively creating a two-dimensional (2D) nematic cortex. Individual kinesin motors, fueled by energy from adenosine triphosphate (ATP) hydrolysis, processively move along a microtubule backbone at velocities up to $0.8 \mu\text{m/s}$ (27). When bound into multimotor clusters through a biotin-streptavidin linkage, kinesin clusters form cross-links with adjacent microtubules, inducing them to slide relative to each other and generating active extensile stresses (19, 28, 29). We image active nematic vesicles by confocal microscopy (30).

In equilibrium there are multiple defect arrangements that minimize the free energy of a 2D spherical nematic, with the exact configuration depending on the strength of the elastic constants. Under the assumption that the bend and splay elastic moduli are equal, the free energy is minimized when four $+1/2$ defects are located at the corners of a tetrahedron inscribed within the sphere (2, 3, 5). This configuration is favored because defects of the same charge repel each other. Placing them at the corners of a tetrahedron maximizes their separation, thus minimizing liquid crystal distortions. The 3D reconstruction of the surface-bound active nematic reveals the presence of four $+1/2$ disclination defects (Fig. 1), in agreement with theoretical predictions for equilibrium systems and previous experimental observations of spherical nematic shells of finite thickness (4).

Oscillating defect dynamics in active nematic vesicles

At finite ATP concentrations, active energy input provided by kinesin clusters drives the microtubule nematic far from equilibrium, yielding surprising dynamics. In planar nematics active stresses destabilize the homogeneous state (31–33) and generate self-sustained streaming flows, with the continuous creation and annihilation of motile defects that interact through elastic and hydrodynamic forces (19, 21–23). When the nematic film is confined to the surface of a sphere, active

¹Department of Physics, Technische Universität München, 85748 Garching, Germany. ²Institute for Advanced Study, Technische Universität München, 85748 Garching, Germany. ³Department of Physics, Brandeis University, Waltham, MA 02474, USA. ⁴SISSA International School for Advanced Studies, Via Bonomea 265, 34136 Trieste, Italy. ⁵Institut-Lorentz for Theoretical Physics, Leiden University, 2333 CA Leiden, Netherlands. ⁶Physics Department and Syracuse Biomaterials Institute, Syracuse University, Syracuse, NY 13244, USA.

*These authors contributed equally to this work. †Corresponding author. E-mail: abausch@mytum.de

unbalanced stresses drive motility of the four $+\frac{1}{2}$ surface-bound disclinations, which leads to streaming flows of the entire vesicle (Fig. 1 and movie S1). The dynamics of spherical active nematics is simpler than that of their planar counterpart, as the four $+\frac{1}{2}$ defects on spherical nematics never disappear and their lifetime is limited only by the vesicle stability. Furthermore, the spatial confinement used in our experiments suppresses the production of additional defect pairs, thus providing a unique opportunity to study the dynamics of a few isolated interacting defects in a controlled way. We speculate that the defect proliferation seen in planar nematics does not occur in our vesicles because they are too small. In all cases, the vesicles' diameter is well below the length scale ℓ_a at which the homogeneously ordered system is unstable to bend deformations. For microtubule-based planar active nematics, ℓ_a is estimated to be $\sim 100 \mu\text{m}$ (29).

Similar to the equilibrium case, the repulsive elastic interactions between four $+\frac{1}{2}$ disclinations in an active spherical nematic normally favor a tetrahedral defect configuration (2, 3, 5). In active systems, however, the asymmetric shape of comet-like $+\frac{1}{2}$ disclinations also generates active stresses and associated flows that in turn drive defect motion. For extensible systems, defects are propelled at constant speed toward the head of the comet (Fig. 1C) (21). It is not possible for the four defects to simultaneously minimize elastic repulsive interactions and move with a prescribed velocity determined by the ATP concentration while keeping their relative distance constant. As a result, defects move along complex spatiotemporal trajectories. To elucidate this emergent dynamics, we imaged the time evolution of active

vesicles by confocal microscopy and traced the 3D position of the individual defects (Fig. 1 and movie S1). At any given time, the positions of the four defects are described by the variables α_{ij} , which denote the angle between radii from the vesicle center to each of the six defect pairs ij (Fig. 2A). For a tetrahedral configuration, all six angles are $\alpha_{ij} = 109.5^\circ$, while for a planar configuration $\alpha_{12} = \alpha_{23} = \alpha_{34} = \alpha_{41} = 90^\circ$ and $\alpha_{13} = \alpha_{24} = 180^\circ$ (and permutations), resulting in an average angle of $\langle \alpha \rangle_{\text{planar}} = \frac{1}{6} \sum_{i < j=1}^4 \alpha_{ij} = 120^\circ$ (Fig. 2A). The temporal evolution of all six angles reveals a clear pattern of defect motion (Fig. 2B). For example, at time $t = 602$ s, two angles assume a large value near 180° while the other four are $\sim 90^\circ$, indicating a planar configuration. Forty-three seconds later, this configuration switches to a tetrahedral configuration in which all angles are equal (Fig. 2D). Observations on longer time scales demonstrate that the defects repeatedly oscillate between the tetrahedral and planar configurations, with a well-defined characteristic frequency of 12 mHz (Fig. 2C). The frequency is set by the motor speed and the size of the sphere, and can be tuned by the ATP concentration, which determines the kinesin velocity (fig. S1) (27).

Particle-based theoretical model describes oscillatory dynamics of active nematic vesicles

The oscillatory dynamics of spherical nematics can be described by a coarse-grained theoretical model. As shown recently, $+\frac{1}{2}$ defects in extensible nematics behave as self-propelled particles with velocity v_0 proportional to activity and directed along the axis of symmetry \mathbf{u} (Fig. 3A and fig. S2) (10). Each defect is then characterized by

a position vector on the sphere $\mathbf{r}_i = \mathbf{r}_i(\theta, \varphi)$, where θ and φ are the spherical coordinates, and a unit vector $\mathbf{u}_i = (\cos \psi_i, \sin \psi_i)$ describing the orientation of the comet axis and directed from the tail to the head. In local coordinates $\mathbf{u}_i = \cos \psi_i \mathbf{e}_{\theta i} + \sin \psi_i \mathbf{e}_{\varphi i}$, where $\mathbf{e}_{\theta i}$ and $\mathbf{e}_{\varphi i}$ are unit vectors in the latitudinal and longitudinal directions, respectively, and ψ_i is the local orientation (fig. S3). Adapting the planar translational dynamics to the curved surface of the sphere, and augmenting it with the dynamics of orientation, the equations of motion of each defect are given by the overdamped Newton-Euler equations for a rigid body

$$\zeta_t \left(\frac{d\mathbf{r}_i}{dt} - v_0 \mathbf{u}_i \right) = \mathbf{f}_i \quad (1)$$

$$\zeta_r \frac{d\psi_i}{dt} = M_i \quad (2)$$

where $\mathbf{f}_i = -dE/d\mathbf{r}_i$ and $M_i = -dE/d\psi_i$ are the force and torque on the i th defect due to the

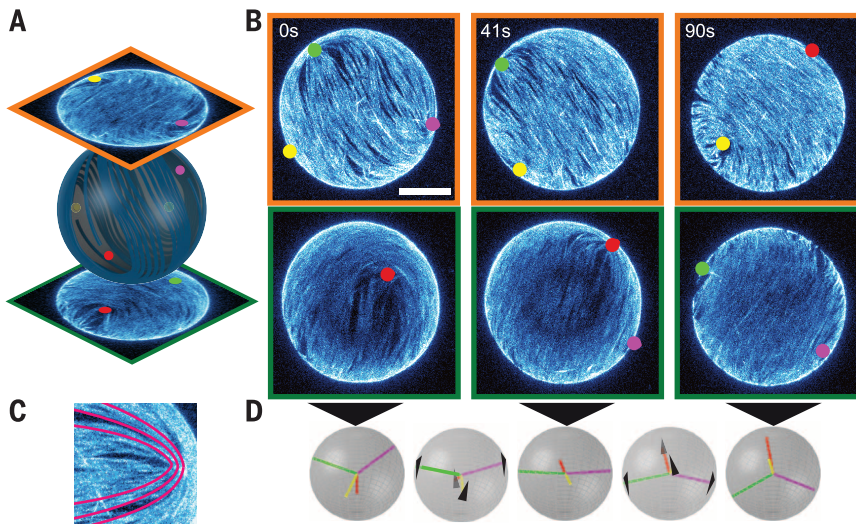


Fig. 1. Defect dynamics of an active nematic film on the surface of a spherical vesicle. (A) Hemisphere projection of a 3D confocal stack of a nematic vesicle. The positions of four $+\frac{1}{2}$ disclination defects are identified. (B) Time series of hemisphere projections over a single period of oscillation in which the four defects switch from tetrahedral ($t = 0$ s) through planar ($t = 41$ s) and back to tetrahedral ($t = 90$ s) configurations. Scale bar, $20 \mu\text{m}$. (C) Comet-like $+\frac{1}{2}$ disclination defect with schematic of the orientation of the nematic director (red lines). (D) Schematic of the defect configurations at the time points of (B) and intermediate times ($t = 24$ s, $t = 65$ s). The black arrowheads indicate the direction of defect motion.

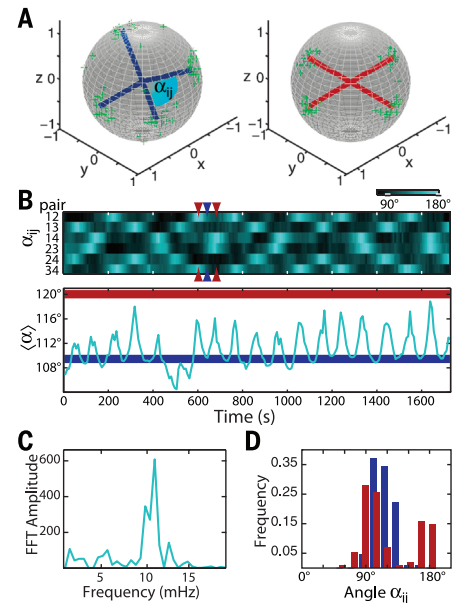


Fig. 2. Oscillatory dynamics of topological defects. (A) Tetrahedral (blue) and planar (red) defect configurations. The green scatterplots show the measured positions of the defects on the unit sphere at the extremal configurations. (B) Top: Kymograph showing the time evolution of angular distances α_{ij} of all six defect pairs [as indicated in (A)]. Bottom: The average angle oscillates between the tetrahedral configuration ($\langle \alpha \rangle = 109.5^\circ$; blue line) and the planar configuration ($\langle \alpha \rangle = 120^\circ$; red line). An exemplary transition between the two configurations is indicated by the colored arrowheads ($t = 602$ s, $t = 643$ s, $t = 684$ s). (C) Power spectrum of $\langle \alpha \rangle$. The peak at 12 mHz is associated with tetrahedral-planar oscillations. FFT, fast Fourier transform. (D) Distributions of angles α_{ij} . Gaussian fits return angles of $109^\circ \pm 13^\circ$ for the tetrahedral configuration (blue) and $90^\circ \pm 12^\circ$ and $163^\circ \pm 9^\circ$ for the planar configuration (red).

repulsive interactions with the other three, with E the elastic energy of the defects, and ζ_t and ζ_r are translational and rotational frictions, respectively (30). The dynamical equations are solved numerically on the sphere, with defects initially randomly spaced along the equator and with random orientations. In equilibrium $v_0 = 0$ and the defects relax toward the minimum of their potential energy, with the four defects sitting at the vertices of a regular tetrahedron (Fig. 3B and fig. S4).

In the presence of activity, a finite v_0 allows the defects to escape from their minimal-energy con-

figuration. This leads to an oscillatory dynamics characterized by a periodic motion of the defects between two symmetric tetrahedral configurations (Fig. 3, C and E), passing through an intermediate planar one (Fig. 3D). The oscillations arise from the competition between the active force $\zeta_r v_0 \mathbf{u}_i$ and the elastic force \mathbf{f}_i . The period is determined by the sum of the time scales for the defect to move uphill and downhill in the energy landscape (Fig. 3F, fig. S5, and movie S2). The period of the oscillations is equal to the time required for a defect to perform a

full revolution around the sphere axis; thus, $T \approx 2\pi R/v_0$ and the frequency increases linearly with activity (fig. S6). Oscillations occur if the rotational dynamics is fast relative to the translational dynamics. For the defects to overshoot when they approach the minimum in the energy landscape, they need to quickly reorient before being attracted back into the energy minimum (fig. S7). The dynamics of the average angle $\langle \alpha \rangle$ (Fig. 3F) reproduces very closely our experimental findings (Fig. 2B).

Thus, the perpetual oscillatory dynamics of active nematic vesicles results from the interplay of topology, liquid crystalline order, and activity. The spherical topology of the vesicles imposes the existence of exactly four $+\frac{1}{2}$ defects with particle-like features. The entropic elasticity originating from the local nematic order shapes the energy landscape through which the defects move. Finally, activity powered by ATP hydrolysis fuels the defect motion. The outlined mechanism leads to robust oscillatory dynamics that survives the presence of noise, which is inevitable in the experimental system.

Active nematic cortex drives large-scale vesicle shape changes

The flexibility of the encapsulating vesicle allows us to study the uncharted regime in which the dynamics of an active nematic cortex couples to a deformable constraining surface (movie S3). To explore the dynamics of this entire regime, we apply a hypertonic stress inducing a water efflux that deflates the vesicle (Fig. 4 and movie S4). The shape of slightly deflated vesicles continuously fluctuates around a mean spherical shape and is characterized by the continuous growth and shrinkage of the major and minor axis of an ellipse, with a periodicity set by the defect transport speed. In addition, these vesicles exhibit four motile protrusions that are tightly coupled to the dynamics of the underlying disclination defects. Deflating the vesicles further causes a marked change in shape: The overall vesicle becomes anisotropic and motile, with filopodia-like protrusions growing in size and reaching lengths of tens of micrometers. The 3D reconstruction of shape-changing flaccid vesicles demonstrates the existence of only four protrusions (Fig. 4B), this number being determined by the fundamental topological constraints. Reswelling the vesicle causes the amplitude of the shape deformations to continuously decrease, the protrusions to vanish, and the vesicle to recover its initial spherical shape.

The other parameter that critically affects the emergent behavior of spherical nematics is the vesicle diameter (34, 35) (Fig. 5). Decreasing the diameter increases the curvature of surface-bound microtubules and the energetic cost of confining active nematics to a spherical surface. For vesicles with radii larger than 18 μm , we only observe oscillations of four motile $+\frac{1}{2}$ defects (Fig. 5H). For smaller radii, the population of vesicles and the emergent dynamics becomes heterogeneous (Fig. 5I). For example, we observe a dynamical mode in which microtubules form a

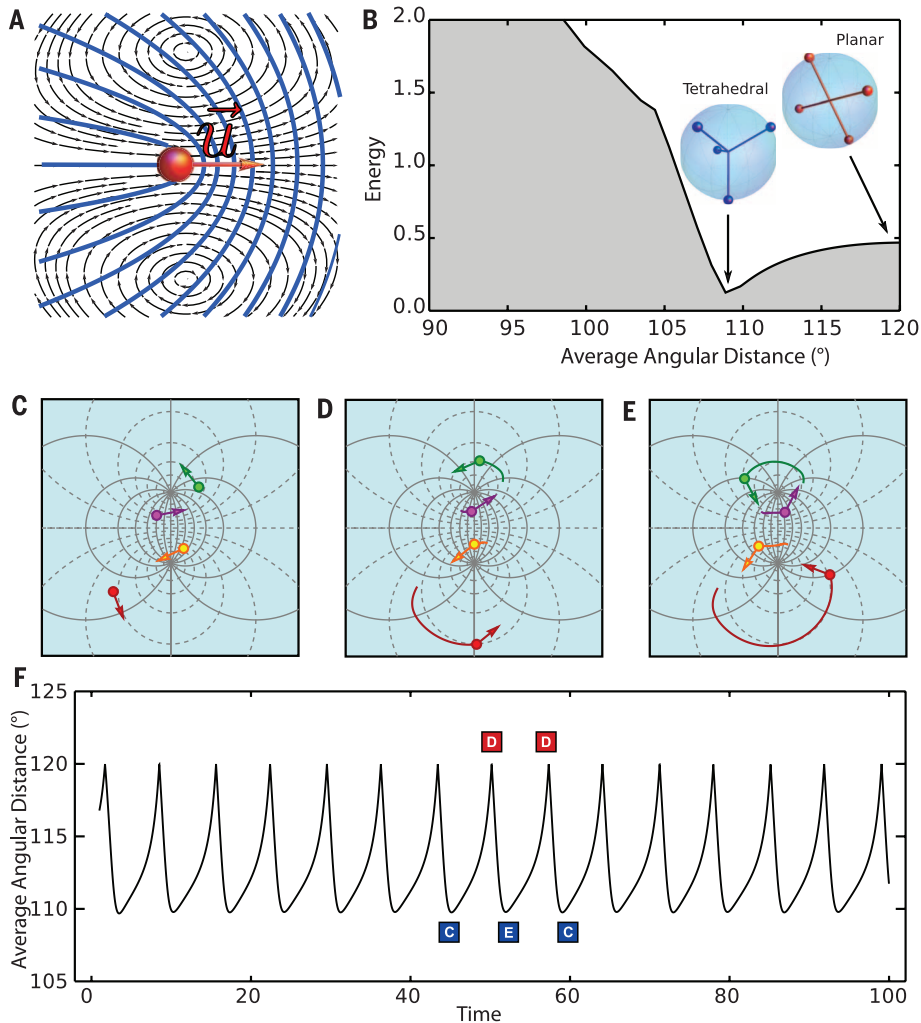


Fig. 3. A theoretical model that describes nematic defects as self-propelled particles predicts oscillatory dynamics. (A) Active $+\frac{1}{2}$ disclinations with an axis of symmetry \mathbf{u} behave as self-propelled particles by generating a local flow (black lines) that convects the defect core toward the head of the comet-like structure described by the director field (blue lines). (B) In the absence of activity, four $+\frac{1}{2}$ sphere-bound disclinations relax toward the minimum of their potential energy, with the four defects sitting at the vertices of a regular tetrahedron. (C to E) For active nematics, the defects undergo a self-organized periodic motion: Starting from a passive equilibrium tetrahedral configuration (C), they pass through a planar configuration (D) on the way to another tetrahedral configuration (E) and then back again periodically. (F) The average angular distance $\langle \alpha \rangle$ as a function of time with asymmetric oscillations between a tetrahedral state [i.e., $\langle \alpha \rangle = 109.5^\circ$, shown in (C) and (E)] and a planar state [i.e., $\langle \alpha \rangle = 120^\circ$, shown in (D)]. The energy landscape reveals a minimum for the tetrahedral configuration and a maximum for the planar one. The average angle $\langle \alpha \rangle$ does not distinguish between the two equivalent alternating tetrahedra shown in (C) and (E). When described in terms of this coordinate, the dynamics oscillates from the minimum of the plot in (B) to the maximum, then back to the same minimum.

rotating ring around the equator of a spherical vesicle (Fig. 5A). The diameter of the microtubule ring increases because of extensile forces driven by molecular motors. To satisfy the spherical confinement the ring eventually buckles out of the equatorial plane, forming a saddle shape

configuration which initiates the formation of the four $+1/2$ defects. The defects collide pairwise and fuse, such that a new ring is formed (Fig. 5, C and D, and movies S5 and S6). By this mechanism, the vesicle switches between the ring structure and the structure characterized by four

$+1/2$ defects (Fig. 5B). For the same parameters we also find that stiff microtubules can deform the vesicle, forming a spindle-like structure with two $+1$ defects at the spindle poles. Structurally, spindle-like vesicles resemble the isotropic-nematic tactoids found in equilibrium liquid crystals (Fig.

Fig. 4. Vesicle shape changes driven by defect dynamics. A 10% hypertonic stress is applied at $t = 5.2$ min to provide an excess membrane area. **(A)** Confocal images showing the z-projection of the vesicle shape, with corresponding 3D schematics shown in **(B)**. Starting from a spherical nematic vesicle with four $+1/2$ defects ($t = 5$ min), four dynamic protrusions grow from the defect sites while the vesicle slowly deswells. At $t = 78$ min, the vesicle reswells and the protrusions decrease in size and eventually disappear. **(C)** Bottom: The amplitude of shape deformations increases over time, as shown by the plot of the vesicle aspect ratio (ratio of major to minor ellipse axis), reaching a maximum value of 1.6 at $t = 75$ min. Restoring vesicle volume \tilde{V} by applying a hypotonic stress at $t = 78$ min inverts the effect, suppressing shape fluctuations. Red arrowheads denote when osmotic stresses are applied. Top: Estimate of the time evolution of \tilde{V} .

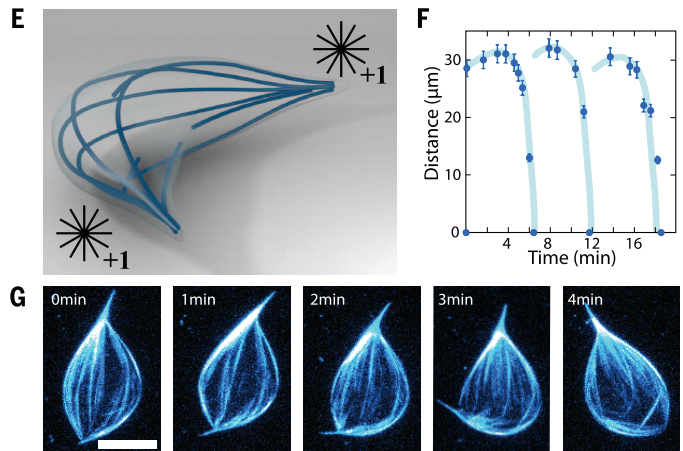
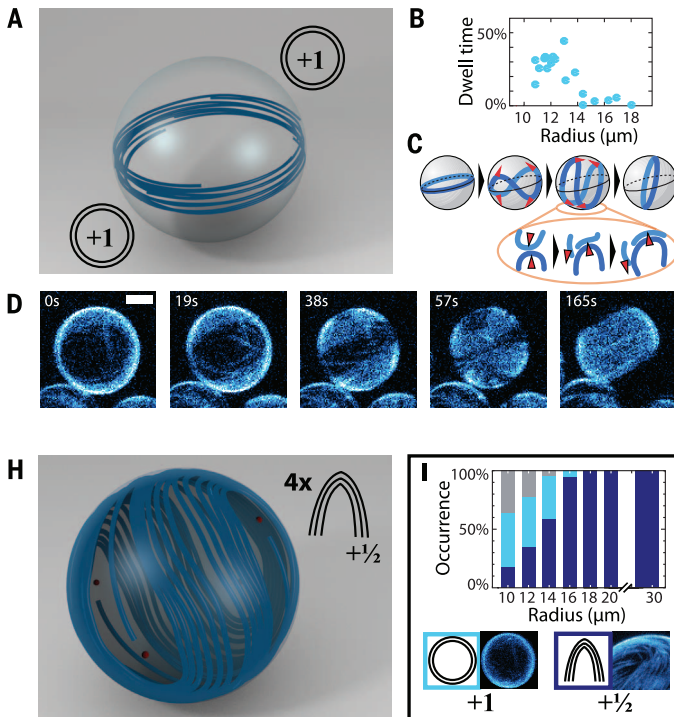
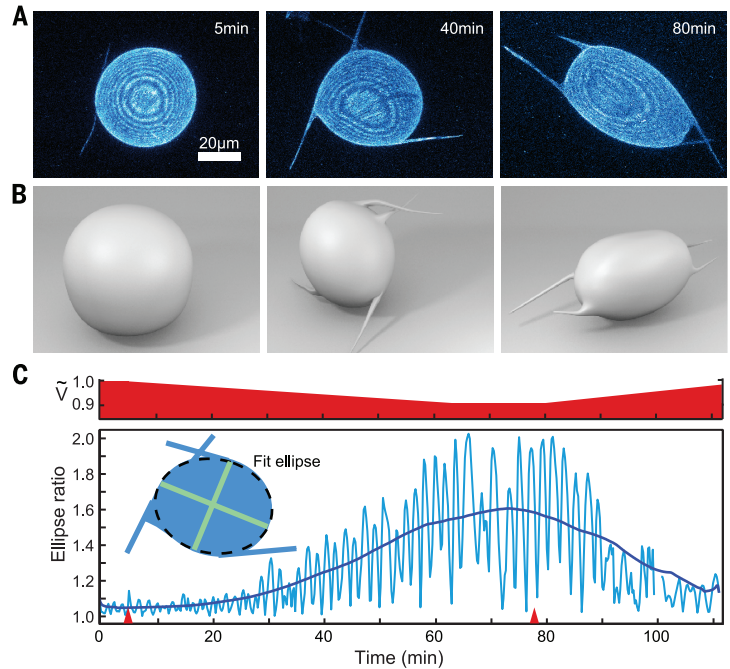


Fig. 5. Size-dependent morphology and dynamics of flexible nematic vesicles. **(A to D)** Ring-mode vesicle. **(A)** Microtubule bundles arrange in a ring around the equator. **(B)** Fraction of time spent by the vesicles in the ring configuration. **(C)** Schematic illustrating the transition between the ring and the four $+1/2$ defect configuration. The corresponding z-projected confocal images for this sequence are shown in **(D)**. **(E to G)** Spindle-like vesicle. **(E)** Each pole contains a $+1$ aster-like defect. **(F)** Temporal evolution of the distance between the two $+1$ aster-like defects. While extending, the microtubule bundles buckle and the two $+1$ protrusions fold on each other. This results in cycles of microtubule extension, buckling, and folding (light

blue lines are guides to the eye). A sequence of confocal images illustrating this dynamics is shown in **(G)**. **(H)** Schematic of a large spherical vesicle exhibiting four $+1/2$ defects. **(I)** Types of dynamics. The histogram shows the percentage of vesicles displaying a defect configuration as a function of the radius (total count = 168). For radii above $18 \mu\text{m}$, all the vesicles exhibit the four $+1/2$ defect configuration shown in **(H)**. For radii in the range 10 to $18 \mu\text{m}$, vesicles that undergo continuous transitions between four $+1/2$ defect (blue) and ring (cyan) configurations [shown in **(A)**] are found. The color code for the defect topology is shown in the pictograms; some cases remain uncharacterized because of resolution limitations. Scale bars, $8 \mu\text{m}$.

5E) (36). Active spindle-like vesicles also exhibit interesting dynamics. Taking advantage of the excess membrane area stored in the membrane tension, the constituent extensile microtubule bundles push outwardly to extend the spindle poles. At a critical bundle length, the connectivity of the constituent microtubule bundles in the central spindle region decreases and the spindle becomes unstable, buckles, and folds into a more compact shape. At this point, the microtubules start extending again, and the cycle of vesicle extension, buckling, folding, and reextension repeats multiple times (Fig. 5, F and G, and movie S7). It is also possible to observe vesicles that transition between spindle and ring structures (fig. S8 and movie S8).

Our results demonstrate how combining active matter with topological constraints yields structures and dynamics that cannot be observed in conventional equilibrium systems (37–40). Specifically, we have shown that confining active nematic films onto the surface of a sphere suppresses defect generation and yields a robust and tunable oscillatory dynamics that is well described by a coarse-grained theoretical model. Furthermore, confinement and the constraints imposed by topology simplify the complex dynamics of planar active nematics that exhibit complex chaotic spatiotemporal behavior.

REFERENCES AND NOTES

1. L. S. Penrose, *Nature* **205**, 544–546 (1965).
2. T. C. Lubensky, J. Prost, *J. Phys.* **2**, 371–382 (1992).
3. D. R. Nelson, *Nano Lett.* **2**, 1125–1129 (2002).
4. T. Lopez-Leon, V. Koning, K. B. S. Devaiah, V. Vitelli, A. Fernandez-Nieves, *Nat. Phys.* **7**, 391–394 (2011).
5. H. Shin, M. J. Bowick, X. Xing, *Phys. Rev. Lett.* **101**, 037802 (2008).
6. V. Vitelli, D. R. Nelson, *Phys. Rev. E* **74**, 021711 (2006).
7. P. Poulin, H. Stark, T. C. Lubensky, D. A. Weitz, *Science* **275**, 1770–1773 (1997).
8. I. Musevic, M. Skarabot, U. Tkalec, M. Ravnik, S. Zumer, *Science* **313**, 954–958 (2006).
9. A. R. Bausch *et al.*, *Science* **299**, 1716–1718 (2003).
10. W. T. M. Irvine, V. Vitelli, P. M. Chaikin, *Nature* **468**, 947–951 (2010).
11. C. P. Lapointe, T. G. Mason, I. I. Smalyukh, *Science* **326**, 1083–1086 (2009).
12. B. Senyuk *et al.*, *Nature* **493**, 200–205 (2013).
13. I. H. Lin *et al.*, *Science* **332**, 1297–1300 (2011).
14. J. A. Moreno-Razo, E. J. Sambriski, N. L. Abbott, J. P. Hernández-Ortiz, J. J. de Pablo, *Nature* **485**, 86–89 (2012).
15. P. Lipowsky, M. J. Bowick, J. H. Meinke, D. R. Nelson, A. R. Bausch, *Nat. Mater.* **4**, 407–411 (2005).
16. G. Meng, J. Paulose, D. R. Nelson, V. N. Manoharan, *Science* **343**, 634–637 (2014).
17. U. Tkalec, M. Ravnik, S. Čopar, S. Žumer, I. Mušević, *Science* **333**, 62–65 (2011).
18. S. Zhou, A. Sokolov, O. D. Lavrentovich, I. S. Aranson, *Proc. Natl. Acad. Sci. U.S.A.* **111**, 1265–1270 (2014).
19. T. Sanchez, D. T. N. Chen, S. J. DeCamp, M. Heymann, Z. Dogic, *Nature* **491**, 431–434 (2012).
20. G. Ducloux, S. Garcia, H. G. Yevick, P. Silberzan, *Soft Matter* **10**, 2346–2353 (2014).
21. L. Gomi, M. J. Bowick, X. Ma, M. C. Marchetti, *Phys. Rev. Lett.* **110**, 228101 (2013).
22. S. P. Thampi, R. Golestanian, J. M. Yeomans, *Phys. Rev. Lett.* **111**, 118101 (2013).
23. T. Gao, R. Blackwell, M. A. Glaser, M. D. Betterton, M. J. Shelley, <http://arxiv.org/abs/1401.8059> (2014).
24. J. Palacci, S. Sacanna, A. P. Steinberg, D. J. Pine, P. M. Chaikin, *Science* **339**, 936–940 (2013).
25. M. Abkarian, E. Loiseau, G. Massiera, *Soft Matter* **7**, 4610–4614 (2011).
26. S. Asakura, F. Oosawa, *J. Chem. Phys.* **22**, 1255–1256 (1954).
27. M. J. Schnitzer, S. M. Block, *Nature* **388**, 386–390 (1997).
28. C. Henrich, T. Surrey, *J. Cell Biol.* **189**, 465–480 (2010).
29. T. Surrey, F. Nedelec, S. Leibler, E. Karsenti, *Science* **292**, 1167–1171 (2001).
30. See supplementary materials on Science Online.
31. R. Voituriez, J. F. Joanny, J. Prost, *Europhys. Lett.* **70**, 404–410 (2005).
32. D. Marenduzzo, E. Orlandini, M. E. Cates, J. M. Yeomans, *Phys. Rev. E* **76**, 031921 (2007).
33. R. Aditi Simha, S. Ramaswamy, *Phys. Rev. Lett.* **89**, 058101 (2002).
34. T. S. Nguyen, J. Geng, R. L. B. Selinger, J. V. Selinger, *Soft Matter* **9**, 8314–8326 (2013).
35. M. Elbaum, D. Kuchnir Fygenon, A. Libchaber, *Phys. Rev. Lett.* **76**, 4078–4081 (1996).
36. P. Prinsen, P. van der Schoot, *Phys. Rev. E* **68**, 021701 (2003).
37. E. Abu Shah, K. Keren, *eLife* **3**, e01433 (2014).
38. H. Baumann, T. Surrey, *J. Biol. Chem.* **289**, 22524–22535 (2014).
39. M. Pinot *et al.*, *Curr. Biol.* **19**, 954–960 (2009).
40. E. Tjhung, D. Marenduzzo, M. E. Cates, *Proc. Natl. Acad. Sci. U.S.A.* **109**, 12381–12386 (2012).

ACKNOWLEDGMENTS

Research was supported by ERC-SelfOrg (F.C.K., E.L., A.R.B.), partly by the SFB863 and the Nanosystems Initiative Munich (F.C.K., E.L., A.R.B.), the Institute of Advanced Study-Technical University Munich (Z.D., F.C.K.), NSF grants DMR-1305184 and DGE-1068780 (M.C.M.), and the Soft Matter Program at Syracuse University (M.J.B., M.C.M.). The primary support for work at Brandeis was provided by the W. M. Keck Foundation and NSF-MRSEC-0820492 (T.S., Z.D.). Acquisition of ATP dependence data was supported by the U.S. Department of Energy, Office of Basic Energy Sciences, grant DE-SC0010432TDD (S.J.D., Z.D.). We also acknowledge use of the Brandeis MRSEC optical microscopy facility.

SUPPLEMENTARY MATERIALS

www.sciencemag.org/content/345/6201/1135/suppl/DC1
Materials and Methods
Supplementary Text
Movies S1 to S8

14 April 2014; accepted 30 July 2014
10.1126/science.1254784

NEURODEGENERATION

Poly-dipeptides encoded by the *C9orf72* repeats bind nucleoli, impede RNA biogenesis, and kill cells

Ilmin Kwon,¹ Siheng Xiang,¹ Masato Kato,¹ Leeju Wu,¹ Pano Theodoropoulos,¹ Tao Wang,² Jiwoong Kim,² Jonghyun Yun,² Yang Xie,² Steven L. McKnight^{1*}

Many RNA regulatory proteins controlling pre-messenger RNA splicing contain serine:arginine (SR) repeats. Here, we found that these SR domains bound hydrogel droplets composed of fibrous polymers of the low-complexity domain of heterogeneous ribonucleoprotein A2 (hnRNPA2). Hydrogel binding was reversed upon phosphorylation of the SR domain by CDC2-like kinases 1 and 2 (CLK1/2). Mutated variants of the SR domains changing serine to glycine (SR-to-GR variants) also bound to hnRNPA2 hydrogels but were not affected by CLK1/2. When expressed in mammalian cells, these variants bound nucleoli. The translation products of the sense and antisense transcripts of the expansion repeats associated with the *C9orf72* gene altered in neurodegenerative disease encode GR_n and PR_n repeat polypeptides. Both peptides bound to hnRNPA2 hydrogels independent of CLK1/2 activity. When applied to cultured cells, both peptides entered cells, migrated to the nucleus, bound nucleoli, and poisoned RNA biogenesis, which caused cell death.

Among familial causes of amyotrophic lateral sclerosis (ALS) and/or frontotemporal dementia (FTD), between 25 and 40% of cases are attributed to a repeat expansion in a gene designated *C9orf72*, with an open reading frame (ORF). The hexanucleotide repeat sequence GGGGCC normally present in 2 to 23 copies is expanded in affected patients to 700 to 1600 copies (1, 2). The pattern of genetic inheritance of the *C9orf72* repeat expansion is dominant, and multiple lines of evidence suggest that the repeat expansion causes disease. Two

theories have been advanced to explain repeat-generated toxicity. First, in situ hybridization assays have identified nuclear dots containing either sense or antisense repeat transcripts (3–5), which leads to the idea that the nuclear-retained RNAs might themselves be toxic. More recently, equally clear evidence has been generated that both the sense and antisense transcripts of the GGGGCC repeats associated with *C9orf72* can be translated in an ATG-independent manner (without an ATG start codon) known as repeat-associated non-ATG (RAN) translation (6). Depending on reading frame, the sense transcript of the repeats can be translated into glycine:alanine (GA_n), glycine:proline (GP_n), or glycine:arginine (GR_n) polymers. RAN translation of the antisense transcript of the GGGGCC repeats of *C9orf72* lead to the production of proline:alanine (PA_n), proline:glycine (PG_n), or proline:arginine (PR_n) polymers.

¹Department of Biochemistry, UT Southwestern Medical Center, 5323 Harry Hines Boulevard, Dallas, TX 75390-9152, USA. ²Quantitative Biomedical Research Center, Department of Clinical Sciences, UT Southwestern Medical Center, 5323 Harry Hines Boulevard, Dallas, TX 75390-9152, USA.
*Corresponding author. E-mail: steven.mcknight@utsouthwestern.edu